# Stress Drop Variations in the Region of the 2014 $M_W 8.1$ Iquique Earthquake, Northern Chile

**J. Folesky**[1], **J. Kummerow**[1], **S.A. Shapiro**[1]

[1]Freie Universität Berlin, Department of Geophysics, Berlin, Germany

**Key Points:**

- Comprehensive stress drop distribution for northern Chile
- Corner frequency estimation by spectral ratio approach
- Spatial and temporal variation of stress drop

Corresponding author: Jonas Folesky, jonas.folesky[at]geophysik.fu-berlin.de

## Abstract

We compute stress drops from P and S phase spectra for 972 earthquakes in the source region of the 2014 $M_W$8.1 Iquique megathrust earthquake in the northern Chilean subduction zone. An empirical Green's function based method is applied to suitable event pairs selected by template matching of eight years of continuous waveform data.

We evaluate carefully the influence of all parameters involved in the stress drop estimation, consider the effect of the local velocity structure and apply an empirical linear relation between P and S phase related geometry factors (k values). Data redundancy produced by multiple empirical Green's functions, the combination of P and S phase spectra and a distributed high quality station network leads to a substantial reduction of uncertainty and comparatively robust stress drop estimates. The resulting stress drop values show a well-defined log-normal distribution with a median value of 2.7 MPa, most values range between 0.1 MPa and 100 MPa.

There is no evidence for systematic large scale lateral variations of stress drop. A detailed analysis reveals a slight increase of the median stress drop with distance to the interface, but no increase with depth. This suggests that fault regime and fault strength play a more important role for the stress drop behavior than absolute stresses.

Interestingly, we find a weak time-dependence of the median stress drop, with an increase immediately before the April 1, 2014 $M_W$8.1 Iquique mainshock, a continuous reduction thereafter and a subsequent recovery to normal values after a few weeks.


## Introduction

Stress drop relates the rupture dimension to the seismic moment of earthquakes which makes it a central parameter of earthquake source analysis, having both practical implications, e.g., on high frequency-ground motion, and theoretical ones on the rupture processes of earthquakes in general. The complex nature of earthquake rupture and with it the behavior of stress drop still raise important questions which have not yet been answered conclusively.

Stress drop has been observed to depend on different factors such as depth, stress conditions and tectonic setting (e.g., Sibson, 1974; Kanamori & Anderson, 1975; Venkataraman & Kanamori, 2004; Allmann & Shearer, 2009; Uchide et al., 2014)). Results, however, are not always univocal. For example, Venkataraman & Kanamori (2004) and Uchide et al. (2014) report strong dependence on earthquake depth, while Allmann & Shearer

(2009) find no evidence for a depth dependence. Similarly, multiple studies support the self similarity of the rupture process, which suggests constant stress drop independent of event magnitude (e.g., Abercrombie, 1995; Shearer et al., 2006; Allmann & Shearer, 2009), but more recent studies also report a considerable correlation between stress drop and seismic moment for different source regions (e.g., Abercrombie et al., 2016; Trugman & Shearer, 2017).

The interpretation of results is generally complicated by the inherent problem that individual stress drop estimates often scatter heavily for a given study area, and different techniques and models produce significant variability of stress drop estimates. Even for similar approaches, the parameter choice may introduce systematic changes of the resulting stress drop values. Therefore, at least for comparative studies, it is beneficial when stress drops are calculated in a consistent way for a large number of earthquakes, as applied in Shearer et al. (2006) or Allmann & Shearer (2009).

For large data sets with predominantly small to medium sized earthquakes the only practical way to compute stress drops is from the spectra of the recorded seismograms. There exist two popular approaches. One is the spectral decomposition introduced by Shearer et al. (2006) which uses a global empirical Green's function (EGF) obtained by an iterative stacking procedure. This method was applied both globally (Allmann & Shearer, 2009) and also in more detail to different regions of the world, e.g., in California (Shearer et al., 2006; Goebel et al., 2015; Trugman & Shearer, 2017) and in the Japan subduction zone (Uchide et al., 2014).

A second approach is the spectral ratio technique based on the classical empirical Green's function (EGF) concept (e.g., Frankel, 1982; Mueller, 1985) where individual, well selected partner events are used to clean the earthquake spectrum from contributions of ray path and site response. Different realizations have been applied over the years to a variety of data sets, including borehole, local and regional recordings (Hutchings & Viegas, 2012; Abercrombie, 2014; Abercrombie et al., 2016). Both approaches were compared in a recent study by (Shearer et al., 2019) which concludes that results are comparable if additional constraints on the corner frequencies of the smaller event in the spectral ratios are introduced. The authors emphasize, however, that the most reliable results are achievable by a uniform processing of comprehensive data sets which approves

the subsequent interpretation of internal variations. In this study we follow this guideline.

We study here seismicity in the northern Chilean subduction zone, a region, which experienced two megathrust earthquakes in recent years, i.e., the 2007 $M_W$7.7 Tocopilla event, and the 2014 $M_W$8.1 Iquique event. Despite the occurrence of these two megathrust earthquakes the postulated northern Chilean seismic gap still remains partially unbroken (Schurr et al., 2014; Hayes et al., 2014). The study area has been monitored intensively since 2006 by the IPOC network (IPOC, 2006). Recently, a comprehensive earthquake catalog of over $100,000$ earthquakes for the time period of 2007 to 2017 and based on the IPOC seismic station data was published by Sippl et al. (2018). Detailed studies have analyzed various characteristics of the 2007 Tocopilla and 2014 Iquique earthquakes, (e.g., Schurr et al., 2012; Fuenzalida et al., 2013; Schurr et al., 2014; Hayes et al., 2014), their foreshock and aftershock behavior (Ruiz et al., 2014; Cesca et al., 2016; Hainzl et al., 2019), ground motion and locking in pre-, inter- and post-seismic phases (Li et al., 2015; Hoffmann et al., 2018; Moreno et al., 2018), fluid-migration and velocity ratios (Bloch, John, et al., 2018), event mechanisms (Cesca et al., 2016), and source characteristics such as directivity (Folesky, Kummerow, & Shapiro, 2018) and corner frequency and radiated energy (Derode & Campos, 2019).

One still missing, essential aspect is a comprehensive analysis of stress drop. While the region has been covered by few global stress drop studies which are methodically confined to large earthquakes (Allmann & Shearer, 2009; Ye et al., 2016) the distribution of stress drop for small to medium sized seismicity is still poorly known. Only single studies report for small numbers of particular events in the Iquique region (Derode & Campos, 2019) and in the Tocopilla region (Lancieri et al., 2012).

Simultaneously, the existing data set from northern Chile provides an ideal condition because of its long time span, its large spatial extent, the different seismically active units covered (plate interface, upper crust, oceanic crust and mantle, see Sippl et al. (2018)) and in particular the recorded intense seismicity related to the fore- and aftershock series of the 2007 Tocopilla event and the 2014 Iquique event.

In this study, we present a workflow which is adapted to the consistent analysis of stress drops for large data sets by relying on a spectral ratio approach similar to Abercrombie (2014) or Huang et al. (2016). We focus on the particularly rich seismicity data in and around the rupture domain of the 2014 Iquique event (Figure 1). We first describe

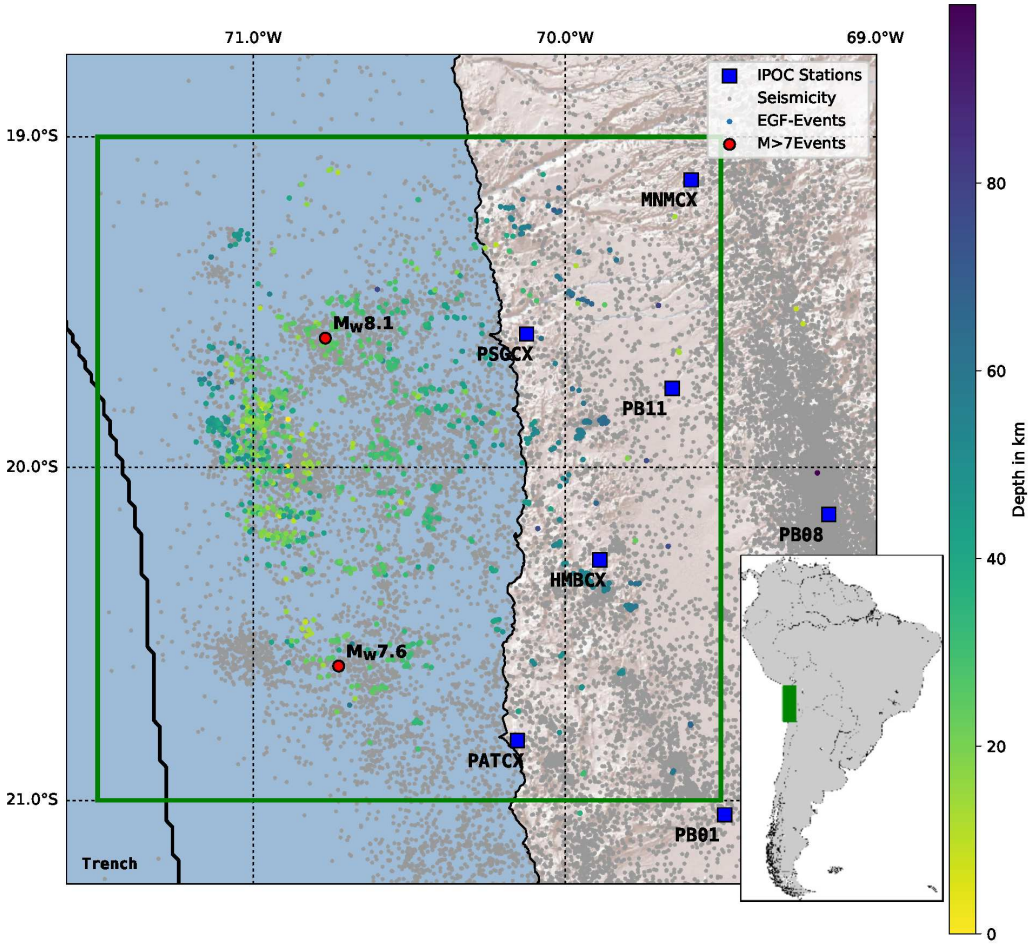


**Figure 1.** Map showing the research area in northern Chile. The 3201 events used in this study are color coded according to their depth. Events from the catalog of Sippl et al. (2018) are shown in grey. IPOC broadband permanent stations are shown by blue squares. Epicenters of the $M_W$ 8.1 2014 Iquique event and its $M_W$ 7.6 largest aftershock are plotted in red.

the method and how we apply it to our data. We discuss the influence of uncertainties introduced by the EGF event selection, the signal bandwidth, the spectral model used, the applied k parameters, the seismic velocity model, smoothing, and seismic moment. We complement this evaluation by an analysis of the robustness of the obtained corner frequencies. We then study the spatial distribution and temporal evolution of the stress drops.

## Catalog and Data

We use the seismic broadband recordings of the Integrated Plate Boundary Observatory Chile (IPOC). The network extends in north to south direction over a length of about 700 $km$ between 17.6°S and 24.6°S. This study focuses on the subregion 19-21°$S$ and 69.5-71.5°$W$ which is shown in Figure 1 by a green square. Event origin times, P and S arrival time picks and event locations are taken from the catalog by Sippl et al. (2018) that consists of more than 100,000 double-difference relocated events. The corresponding 100 $Hz$, three-component waveform data were accessed through the EIDA web service of GFZ Potsdam (Bianchi et al., 2015).

In this region, seismicity occurs mainly on the interface between the subducting oceanic Nazca plate and the overlying South American plate, with some additional events in the overlying continental crust and also in an active deeper band, located about 20 to 25 $km$ below the interface within the oceanic mantle.

## Method

We apply an empirical Green's function (EGF) method called the spectral ratio approach, where an EGF is a smaller earthquake with similar location and focal mechanism as the target event. The method can be used to extract detailed source properties of the target event such as source time function or directivity without explicit knowledge of path effects or attenuation (cf. Hutchings & Viegas, 2012, for an overview). We apply an approach that is based on the fit of an appropriate source model to the spectral ratio between target event and EGF event in order to identify the corner frequency of the larger event from the event pair. The procedure is described in the following.

### Selection of Suitable Empirical Green's Functions (EGF)

We start the analysis by selecting 9071 catalog events from the earthquake catalog by Sippl et al. (2018) which are located in the study area and which are well recorded by the neighboring IPOC stations (cf. Figure 1). For each catalog event we perform a template matching scan of the continuous waveform data recorded at station PB11 for the years 2008 to 2016. A bandpass from 1 to 4 Hz is applied. The templates have a length of 35 s starting 5 s before P pick and include both P and S wave coda. If the normalized cross-correlation coefficient of $cc = 0.8$ is exceeded, the detected and the template event are defined as a potential event pair. The long cross-correlation time window encompassing both the P and the S phase window ensures the appropriateness of the EGF in terms of co-location and similarity of mechanism of both events (Menke, 1999). Using this procedure we obtain in total $20,484$ event pairs. Most of the EGF events are new detections which were not listed in the catalog before. For further analysis we also require a minimum magnitude difference of $\Delta M \geq 1$. This is computed from the ratio of the peak amplitude values (velocities) for each target event with its corresponding EGF event at station PB11 where $\mathrm{A}_{target}/A_{EGF} \geq 10$. After application of this criterion the number of potential events pairs reduces to 3201 which remain for the analysis. Their locations are highlighted in Figure 1.

### Spectral Ratio and Data Fitting

We apply a spectral ratio approach similar to Abercrombie et al. (2016) and Huang et al. (2016) where the spectrum of a target event is divided by the spectrum of its corresponding EGF event. The resulting spectral ratio can be used to assess the corner frequency of the larger and the smaller event as well as the ratio of their seismic moments. In theory this can be described by the ratio of two events $i = 1, 2$ under the assumption of a specific spectral source model, e.g., the one of Brune (1970) or Boatwright (1980):

$$\frac{u_1(f)}{u_2(f)} = \frac{\Omega_1}{\Omega_2} \left( \frac{1 + (f/f_{c_2})^{\gamma n}}{1 + (f/f_{c_1})^{\gamma n}} \right)^{\frac{1}{\gamma}}, \tag{1}$$

where $u_i$ is the displacement, $\Omega_i$ is proportional to the seismic moment $M_{0i}$, $f_{ci}$ is the corner frequency and n the spectral falloff rate while $\gamma$ depends on the assumed source model (e.g., $\gamma = 1$ for the Brune model, $\gamma = 2$ for the Boatwright model). The latter model of Boatwright (1980) predicts a sharper cornered source spectrum, and when applied to our data we find a consistently lower RMS compared to the model of Brune (1970).

Therefore, the subsequent analysis is performed using the Boatwright model with $\gamma = 2$. In principal it is possible to allow for variations of the falloff rate n, but this would introduce additional uncertainties into the estimation of the corner frequency (Kaneko & Shearer, 2014). In order to ensure better comparability and to limit the degree of freedom for the fitting (Kaneko & Shearer, 2015), we fix the value to $n = 2$ which matches well our data.

We perform the entire procedure separately for P and S phases. Data are first detrended, integrated to displacement and then bandpass filtered between 0.8 to 40 Hz, all using built-in Obspy functions (Beyreuther et al., 2010). For the P phases, we select a time window starting at 0.5 s before the P phase pick and ending at 1.7 times the catalog based P phase travel time, the approximate S phase arrival. For the S phases, the window is taken relative to this approximate S pick with a 1.7 times longer duration. The minimum duration for both time windows are 10 s and 17 s, respectively. The signal to noise ratio is computed as the ratio of the phase peak amplitude value to the standard deviation of a time window directly preceding the P phase with P phase window length. Only if a threshold value of 3 for the signal to noise ratio is exceeded, the seismogram trace is considered for further analysis (similar to Shearer et al., 2006, 2019).

In a next step the spectra are computed and smoothed. We use the smoothing approach of Konno & Ohmachi (1998) which was developed originally to stabilize the spectral ratio between horizontal and vertical components for computing ground motion characteristics. The method ensures a constant point number in the given frequency bin in order to mitigate the overweight of high frequencies while smoothing (Huang et al., 2016).

The theoretical spectral ratio model (Equation 1) is then fitted to the ratio of the smoothed spectra. We optimize for the parameters $f_{c_1}, f_{c_2}$ and $\Omega_{1/2}$ using the trust region reflective method from scipy curve_fit with the aim to describe the shape of the entire spectral ratio as exactly as possible. For further analysis, however, we only use $f_{c_1}$, henceforth denoted as $f_c$. The procedure is looped over all receivers and traces. For each data trace the fit is performed independently. We require a minimum of four estimates of $f_c$ for each event pair in order to proceed with the stress drop estimation. If sufficient corner frequencies were obtained results are averaged by determining their median. The median is a robust measure to minimize the influence of outliers and simultaneously account for possible azimuthal variations of the corner frequency which are to be expected due to the observation geometry and due to a possible source directivity. Such effects

can be significant and are well described in Kaneko & Shearer (2014, 2015). Since the source plane orientation and directivity are unknown, it is not possible to compute take-off angles and differentiate between rupture types. Accordingly, we choose the comparatively robust median value for averaging the individually obtained corner frequency values.

**Computation of Stress Drop**

To compute the stress drop we take the circular source model as derived by Eshelby (1957) and Madariaga (1976) and write:

$$\Delta\sigma = \frac{7\pi\mu\overline{D}}{16r} = \frac{7M_0}{16r^3}, \tag{2}$$

where r is the approximate fault radius, $\overline{D}$ is the average slip on the fault, $\mu$ is the shear modulus, and $M_0$ is the seismic moment. In general, slip and fault dimensions are not easily determined, and we cannot compute the stress drop directly (Kanamori & Anderson, 1975). We therefore resort to a method which derives stress drop from the source displacement spectrum. The approach of Brune (1970) provides a link between source radius and the spherically averaged corner frequency (see also Madariaga, 1976; Kaneko & Shearer, 2014, 2015):

$$f_c = k\frac{\beta}{r}, \tag{3}$$

with the shear wave velocity at the source, $\beta$, and a constant $k$ that relates to the spherical average of the corner frequency for a specific theoretical source model. By combining Equations 2 and 3 the sometimes called 'Brune type' stress drop can be computed

$$\Delta\sigma = \frac{7}{16}\left(\frac{f_c}{k\beta}\right)^3 M_0. \tag{4}$$

We described above the procedure to obtain the value for the spherically averaged corner frequency $f_c$ (Eq. 1). In order to compute the stress drop, we rely on additional information for the other parameters.

Münchmeyer et al. (2020) provide a refined and consistent magnitude catalog for the data set of Sippl et al. (2018). We derive the seismic moment from the moment magnitude given in their catalog by using the standard relation ($M_W = 2/3(log(M_0)-9.1)$).

Because of the large spatial extent of our event distribution, shear wave velocities vary considerably, and we use the extrapolated 2D velocity model section at 20°S of the

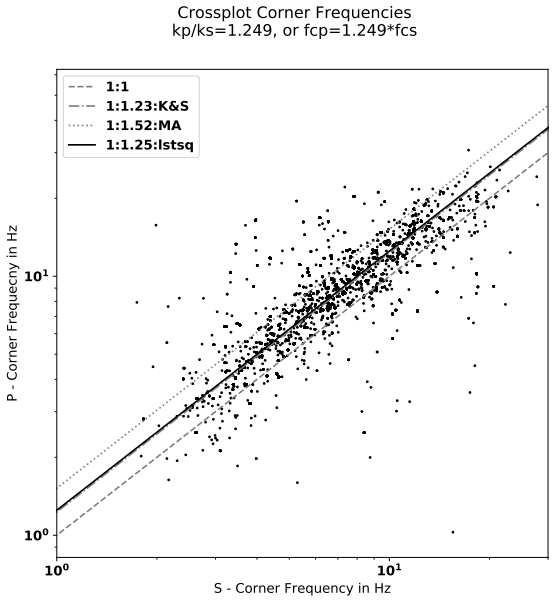


**Figure 2.** P phase based versus S phase based corner frequencies. The four different lines are the 1:1 line, the 1:1.23 line illustrative for one of the rupture models of Kaneko & Shearer (2014) where $v_r/\beta = 0.7$, 1:1.52 the value obtained by Madariaga (1976) for $v_r/\beta = 0.9$, and our estimate 1:1.249 obtained by fitting a least square regression line to the data. Visually, lines 2 and 4 are almost indistinguishable.

velocity model from Bloch et al. (2014) to determine the shear wave velocity individually for each event pair. For the $k$ parameter we take the standard value from Brune (1970): $k_p$ =0.32 for P phases. Following Prieto et al. (2004) and Abercrombie et al. (2016) we estimate the relation of P to S phase derived corner frequencies for our entire data set, as shown in Figure 2. The procedure provides a best fitting ratio of $k_p/k_s = 1.249$ yielding a value of $k_s$ =0.25 for S phases. By choosing both k values accordingly, we obtain comparability of the resulting stress drop values from P and S phases.

When we process the complete data set we find that many target events have not only one P and S phase based stress drop estimate (which was obtained by taking the median over all recording stations), but they may also have additional EGF events. In these cases we collect the results and take the median of all estimates to enhance stability further. We will also make use of the redundancy information from these event families to estimate the robustness of our approach as described in the uncertainty section.

## Data Example

We illustrate our realization of the spectral ratio approach for one event pair in Figures 3 & 4. Figure 3 shows all pre-processed displacement traces available for both events. The selected (here P) phase windows are highlighted in grey. Figure 4 displays the corresponding smoothed spectra, their spectral ratios with the obtained fit curves for the utilized spectral model and the station wise variation of corner frequency with the overall median for the target event. The given stress drop value of $\Delta\sigma = 1.4\,\mathrm{MPa}$ is computed from the median of the individual corner frequencies, which is in this case $f_c = 4.0\,\mathrm{Hz}$. Note also the good consistency between the individual measurements. Additional examples are given in the supplement, including an example based on S phase spectra.

## Uncertainties

In the following, we will discuss the most important sources of uncertainty inherent to the stress drop estimation procedure and compute errors if possible. The absolute error for stress drop measurements are often considerable and a consequence of the constitutive formula for Brune type stress drop estimation, which involves the cubes of the three quantities $f_c$, $\beta$ and k (Equation 2). Data redundancy, however, allows us to analyze the variability of corner frequency measurements, and we will find reasonable relative errors.

The first source of uncertainty is related to the selection of suitable empirical Green's function events. Using inappropriate EGF events would result in reduced validity of the deconvolution procedure to recover the spectra of the target events. We apply a high cross correlation threshold of cc=0.8 measured over a long time window of 35 s. Additionally, we require a minimum magnitude difference of $\Delta M \geq 1$ between target and EGF event. These are comparably rigorous restrictions, and we do not observe any influence on the stress drop estimate by varying the values above these two thresholds, which confirms the observations by Abercrombie (2015) and Abercrombie et al. (2016).

Furthermore, the expected corner frequency must lie well within the recording bandwidth. We discard single component $f_c$ outliers outside of the interval of our bandpass filters. If this leads to less than 4 remaining $f_c$ estimates for one event, the event is entirely disregarded. The range of corner frequencies for the entire data set is between 2 and 25 Hz (cf. Figure 11) and lies comfortably below half the sampling rate of 100 Hz

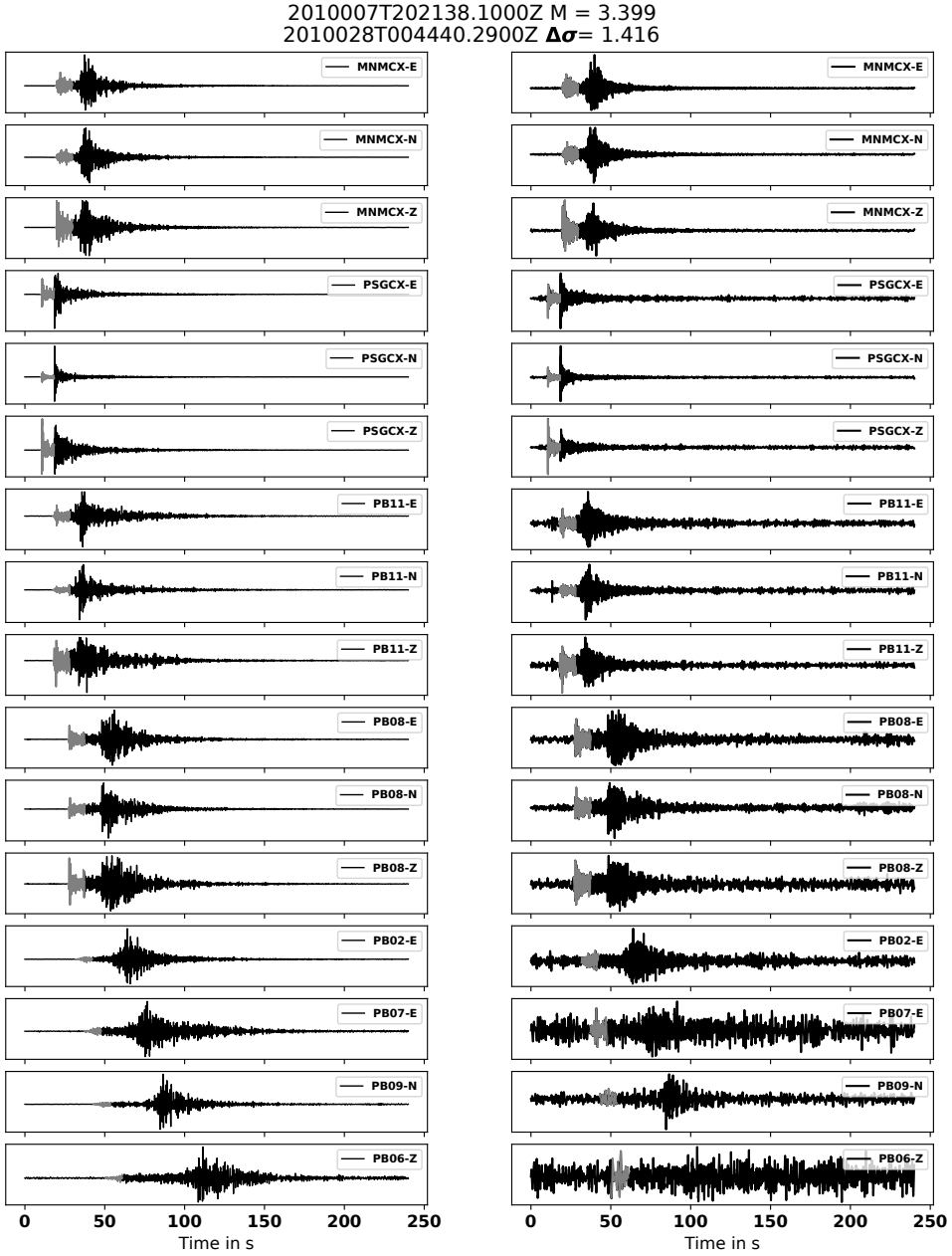


**Figure 3.** Selection of P phase windows for an exemplary event pair. (Left) Pre-processed displacement traces of the target event, (right) pre-processed displacement traces of the smaller magnitude EGF event. Only the traces which comply with our selection criteria are displayed (see Method section). The labels contain station and component names. The P picks are taken from the catalog for the target event and transferred to the EGF event based on the inter event time. The header specifies event origin times, magnitude of the target event, and estimated mean stress drop.

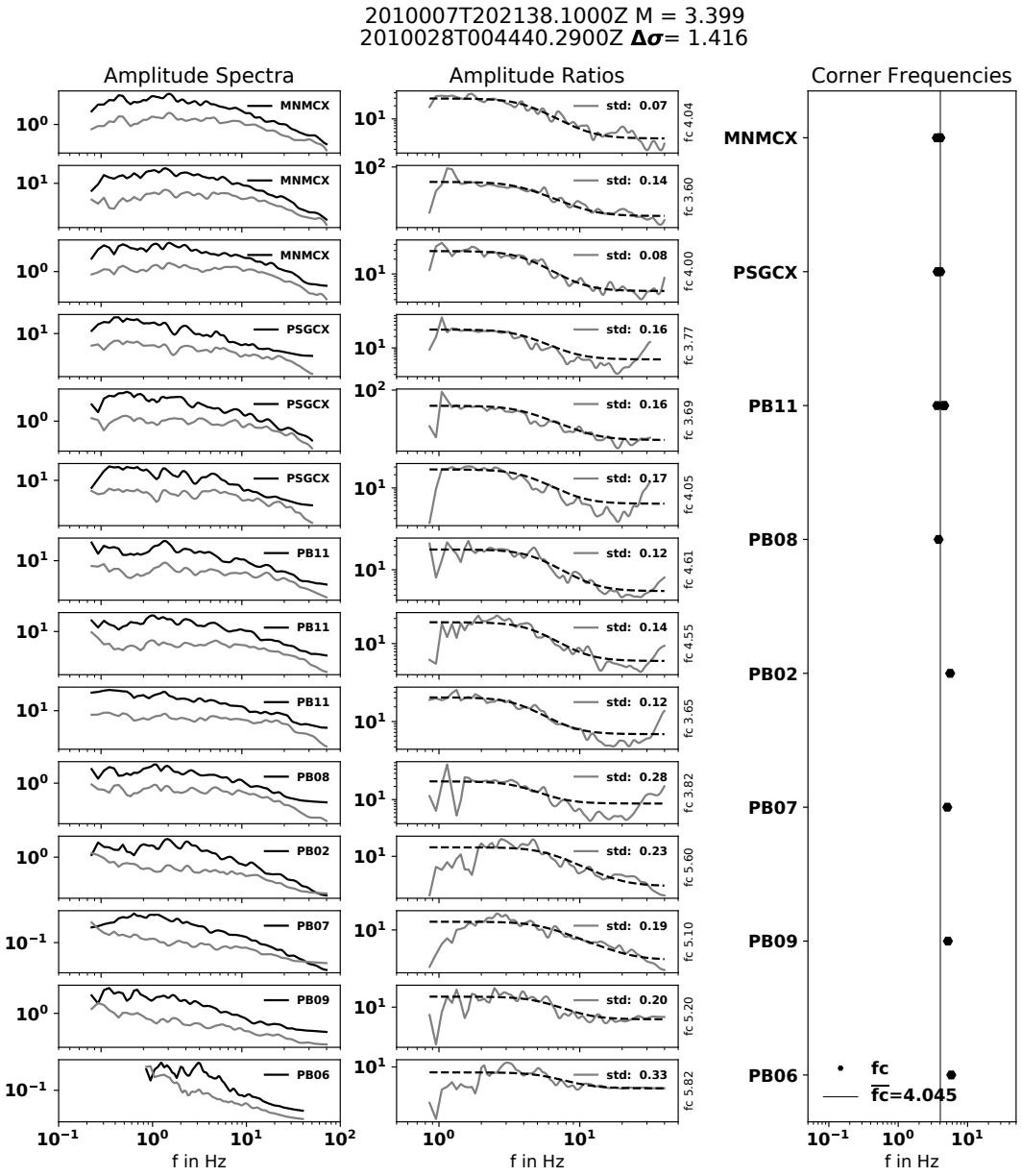


**Figure 4.** Smoothed displacement spectra of the example events from Figure 3 (left). The spectral ratio is computed and the Boatwright spectral model is fitted to the data (center). Corner frequency ($f_c$) and standard deviation (std) are given for each spectrum. The corner frequencies are then plotted station wise to the right where stations are sorted from north to south (right). The median value, $\overline{f_c}$, is indicated by the vertical line and is used for the computation of stress drop. For this event, $f_c$ = 4.0 Hz. The header states event origin times, magnitude of the target event, and estimated stress drop ($\Delta\sigma = 1.4$ MPa).

and also well within our bandpass limits. While we leave it unconstrained, some authors pin $f_{c_2}$ to the maximum frequencies when the bandwidth limits are approached or exceeded (e.g. Shearer et al. (2006); Hardebeck & Aron (2009)) which sometimes seems to enhance results (Shearer et al., 2019).

In order to enhance stability of the computation of the spectral ratio we smooth each spectrum before fitting (Huang et al., 2016). We use the Konno & Ohmachi (1998) smoothing operator to account for the logarithmic distribution of sample points in each smoothing window. We verified that only a minimal, systematic shift of $f_c$ is introduced by the smoothing, using a simple synthetic source spectrum with added Gaussian white noise.

The choice of the spectral model has a systematic influence on the estimated corner frequency. Because of their spectral shapes, the Brune model provides a lower $f_c$ than the Boatwright model. We tested both models and found that the Boatwright model overall describes our data better. We therefore selected it for the analysis. By optimizing additionally for the falloff rate n in Equation 1, it is in principle possible to further improve the fitting and decrease the standard deviation of the parameter $f_c$ while introducing another uncertainty for n itself (Trugman & Shearer, 2017). We refrain from this approach and fix $n = 2$ which makes the results somewhat more comparable (Kaneko & Shearer, 2014). We compute standard deviation values from the curve fit routine for each single station $f_c$ as illustrated in Figure 4 and supplementary Figures 3 & 5. One could use them to apply weighted averages (Abercrombie et al., 2016), but we find that taking the median gives robust results, handles outliers well, and is more intuitive for interpretation.

To evaluate the statistical error of the corner frequency of our analysis we exploit the redundancy of $f_c$ measurements within our data set. Because P and S phase based corner frequencies are computed separately, almost all events have at least two independent estimates. Many events also belong to so called event families for which the target event has two or more associated EGF events. We compute the median corner frequency for each target event from all P and S phase based measurements within an event family and calculate the relative difference of each single estimate to this median value. Figure 5 shows the distribution of relative differences combined for all 942 event families. Counting P and S phase separately, a total of 4126 EGF events were used. The histogram is scaled in order to fit a PDF to the data. The best fitting PDF has exponential shape ($PDF = \lambda e^{-\lambda x}$). We compute the corresponding standard deviation $std =$

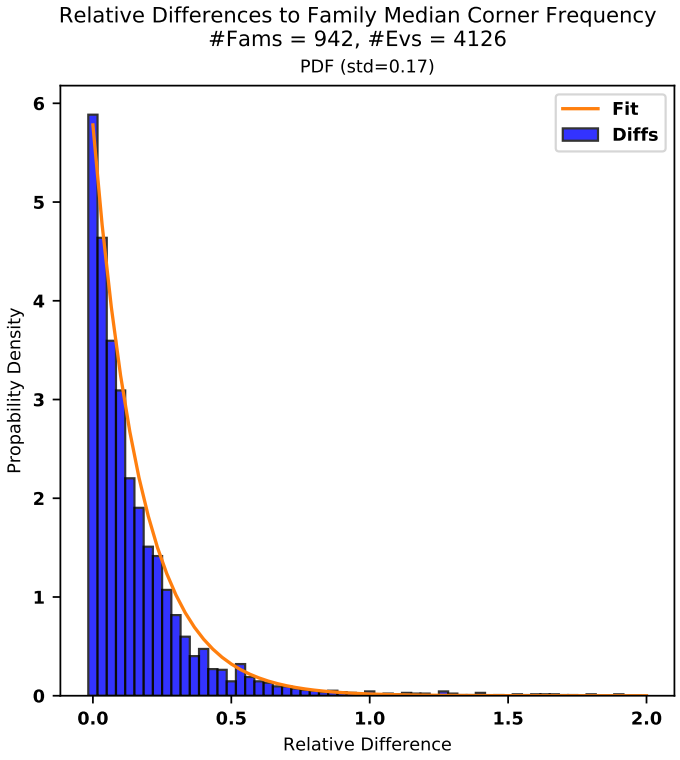


**Figure 5.** Histogram of relative differences to the family- specific median corner frequencies, i.e. for each of the 942 target event one single median is calculated from the existing estimates (in total 4126), and the individual differences are divided by this median. The distribution is normalized and a PDF with exponential shape is fitted to the data.

$1/\lambda = 0.17$. This value compares well with the range of normalized standard deviations for multiple station estimates provided by Abercrombie (2015) (their Figure 4) who explicitly investigated EGF uncertainty factors. We will use the obtained value as an approximate relative error, i.e., $\delta(f_c) = 0.17$.

The true rupture velocity is almost always unknown and poses another source of uncertainty. In the frame of Brune type stress drop estimation it is usually treated in combination with the rupture mechanism and the observation geometry which is expressed by the k value in Equation 2 (Brune, 1970; Sato & Hirasawa, 1973; Madariaga, 1976). Kaneko & Shearer (2014) show in detail that different combinations of $k_s$ and $k_p$ for S and P phase, respectively, can be assigned to different source models and rupture velocities. In principal, k is also station-specific and depends on the takeoff angle under which the ray leaves the source. Figure 2 displays the event wise and spherically averaged corner frequencies of P phase versus S phase for the entire data set. The computed regression line gives the ratio for which both phases provide on average the same stress drop for a given event over the entire data set. According to Kaneko & Shearer (2014) our estimate of $k_p/k_s$=1.249 can be explained by a symmetrically rupturing circular source with a rupture velocity of $v_r = 0.7\beta$. Here, one important assumption is that the available stations provide sufficient measuring points for a robust spherical average. We set thresholds of 24, 12, 8 and 4 minimum single trace $f_c$ measurements required for analysis. No significant changes of the average properties ($k_p/k_s, \overline{f_c}, \overline{\sigma}$) are found when n is varied. For example, $\overline{\sigma}_{n=4} = 2.65\,MPa$ and $\overline{\sigma}_{n=24} = 2.24\,MPa$. In contrast, the regression yields a standard error of $std(k_p/k_s)_{n=4} = 0.73$ which reduces to $std(k_p/k_s)_{n=24} = 0.41$ while $k_p/k_s$ remains approximately constant for variable n. To include as many events as possible in the analysis we chose a minimum number of n=4 as a threshold. Figure 2 demonstrates that the uniform $k_p/k_s$ ratio holds well for the majority of events, but it also indicates differing ratios for some events. This is equally reflected in the relatively large regression standard error of $k_p/k_s$. A possible explanation for this observation are deviations in the rupture characteristics such as rupture mechanism or directivity. Note that he computation of a collective k value for the entire data set presumes that all sources have similarly oriented rupture planes and similar rupture models, which is of course a strong simplification. It is, however, not feasible to work with family specific k values, if orientation, rupture velocities and mechanisms are not well known. We therefore apply the standard value of Brune with $k = 0.32$ and a fixed k ratio.

Next, knowledge of the seismic moment $M_0$ is required to compute the stress drops (Equation 2). We derive it from the moment magnitudes provided by Münchmeyer et al. (2020). Although uncertainties for the magnitudes are very low in their catalog - the authors give standard deviations in the low percentage range - this translates to about ten-fold relative errors for the corresponding seismic moment, i.e., the relative error ranges between 10–30% for most events.

The last parameter in the stress drop computation formula is the shear wave velocity $\beta$. Especially in a subduction zone setting phase velocity may vary significantly on a 10 km scale. It is consequently important to apply the best velocity model available. We obtain $\beta$ from a pseudo 3D velocity model created by Bloch et al. (2014) and use individual values for each target event depending on its location.

In summary, we have discussed here the contributions of the various parameters to the uncertainty in the stress drop estimation. Their effects are different. We fix the model dependent value k, which produces a static shift of absolute values. We also incorporate the velocity structure for the parameter $\beta$, which, if chosen inappropriately, could otherwise introduce artificial heterogeneity of the stress drop distribution. Only $M_0$ and $f_c$ are determined here individually for each event. Their combined relative errors as estimated in this study may produce deviations of maximum a factor of 2-3 from the "true" stress drop value. This is much smaller than the variability of the stress drop values, which ranges over 2–3 orders of magnitude. We conclude that our workflow is reasonably well suited to produce meaningful results and capable of resolving actual variations of stress drop.

## Results & Discussion

The workflow is applied to the entire data set of 3201 events (Figure 1). The analysis yields 2094 P phase based and 2158 S phase based stress drop estimates. These numbers reduce when accounting for the fact that a target event may have multiple EGF events. As explained earlier we combine the P and S phase derived stress drops by fixing the ratio of the k parameters to the previously calibrated value $k_p/k_s = 1.249$ (Figure 2). For each target event we then merge the measurements from P and S phases and from additional EGF events, if existent, by taking the median over all single estimates. This procedure yields stress drop estimates for 972 target events. Their distribution is plotted event wise in Figure 6. The resulting stress drops show a well pronounced log-normal

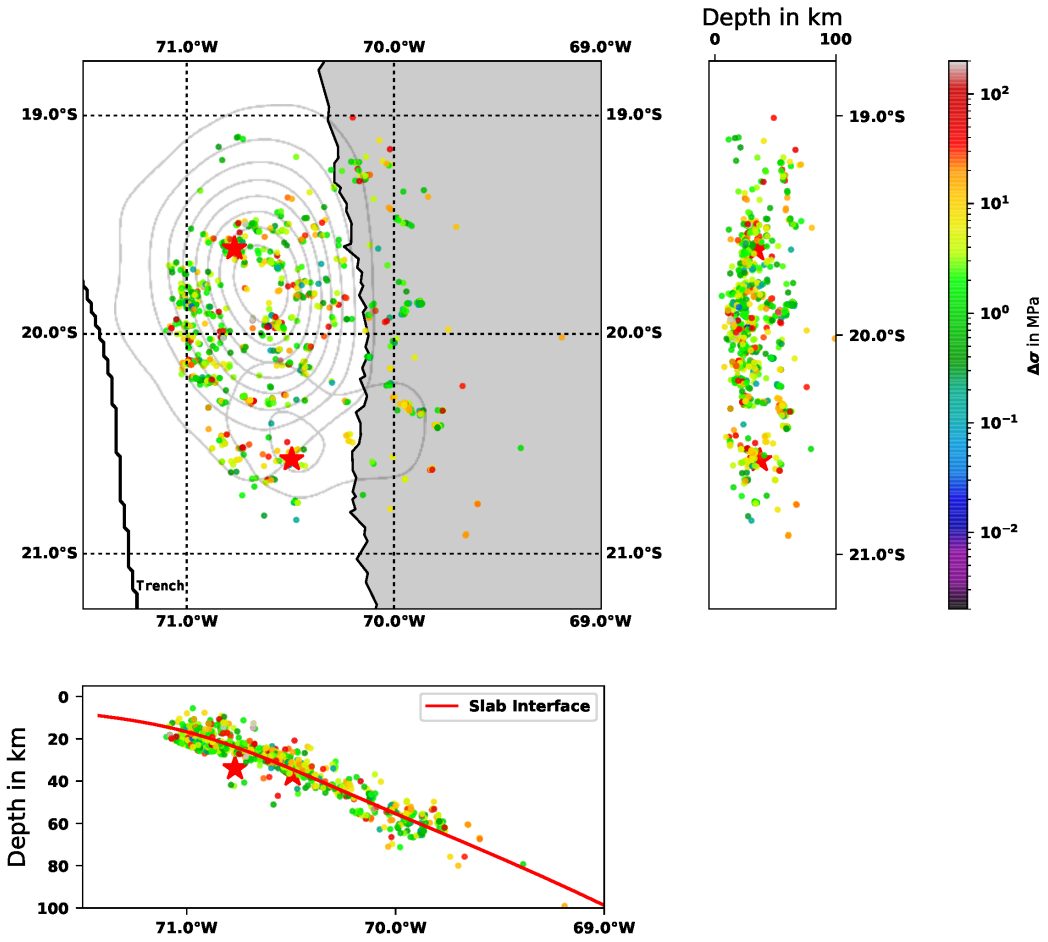


**Figure 6.** Stress drop distribution for 972 target events in map and depth views. Color indicates the stress drop value. The red stars indicate the hypocenters of the $M_W$8.1 Iquique event and the $M_W$7.6 largest aftershock. Underlain is the coseismic slip distribution in 0.5 m increments taken from Schurr et al. (2014). The red line in the west–east depth section delineates the slab interface from Hayes et al. (2012).

distribution with an overall median stress drop of $\Delta\sigma = 2.65\,MPa$ displayed in Figure 7. This value is of the same order as the independently estimated stress drops for the Iquique earthquake, $\Delta\sigma = 7.66\,MPa$, and its biggest aftershock, $\Delta\sigma = 4.28\,MPa$ (Ye et al. (2016)). The stress drop map reveals a heterogeneous distribution. Note that the spectral ratio approach is limited to those subregions only where suitable EGF events exist. Event density is much higher on the part of the interface that lies updip of the maximum slip patch of the 2014 Iquique event. This observation reflects the overall very high updip seismic activity related to the megathrust event. We note that average to low val-

ues (green) dominate here, whereas in some other areas, higher values prevail (orange–red). We attempt to identify regions of characteristic stress drop behavior by dividing the study region into grid cells and computing the median stress drops for each cell, similar to the approach by Uchide et al. (2014). The results are shown in Figure 7. Average values still dominate, but some patches formed by three ore more neighboring cells exhibit increased median values. Among others we identify a small patch of elevated values north of the nucleation point of the $M_w$8.1 main shock, as well as a larger patch of increased values west of the hypocenter of the $M_w$7.6 aftershock, both highlighted by black outlines. When interpreted as stress barriers marked by higher roughness which only eventually were released, they could possibly indicate domains of the interface which inhibited further growth and limited the rupture area of the large Iquique event, as suggested e.g. for the 2011, Tohoku-Oki earthquake by Uchide et al. (2014).

To analyze the spatial dependency further we plot several spatial sections in Figure 8. In addition to the estimated stress drops, the median values for bins of 0.1° width are overlain for better visualization.

In the west–east section, bin values are continuously close to the overall average, with singular elevated values to the east.

The north–south section also shows mainly close to average values except for a few domains of increase, e.g., at 19.4°S and 20.5°S. These correspond to the higher stress drop value patches observed previously and highlighted in the map view. South of 20.5°S, Sippl et al. (2018) identified increased upper plate seismic activity, which was suggested to correlate with a reduced interplate locking (Li et al., 2015; Moreno et al., 2016). We observe here the steady decrease of stress drop, when starting from 20.5°S and progressing towards south, which could corroborate their observation when confirmed with more events further south.

The depth view reveals no clear dependence of stress drop on depth. Median values are fairly stable down to about 45 km depth where they start to decrease, rise back for a few kilometers and then decrease again to the lowest value of the curve (about 0.5 MPa median stress drop). Only below this feature, an increase is observed, which is, however, evidenced by very few events only. These particular events are situated clearly below the interface within the oceanic mantle as can be seen from the depth section in Figure 6 (the lowest, yellow colored events). The increase of stress drop observed here correlates

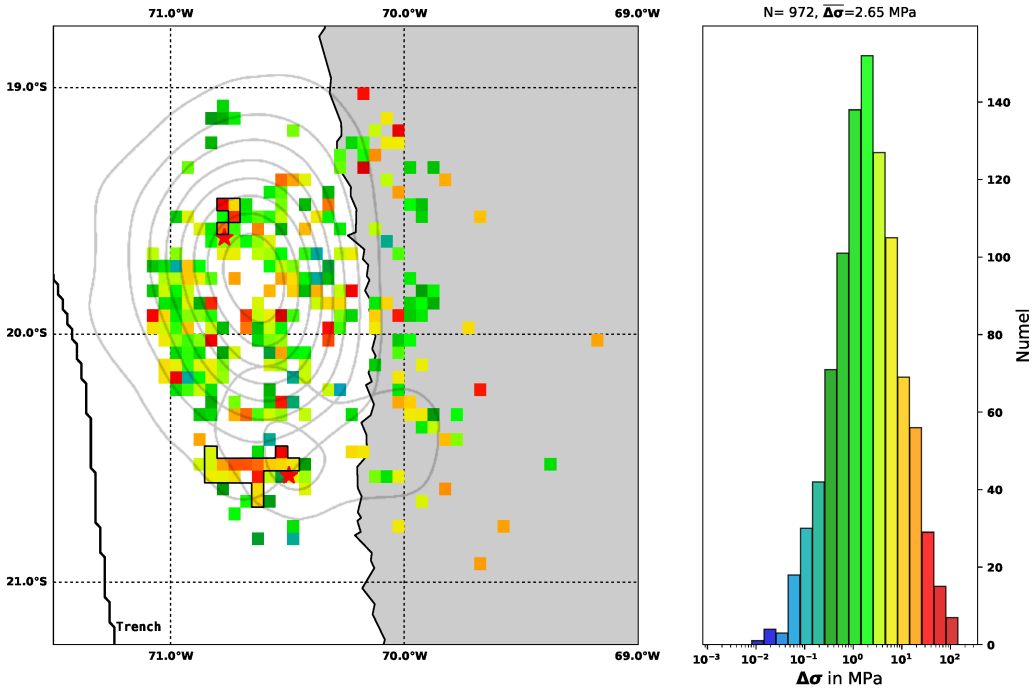


**Figure 7.** Stress drop distribution averaged on a regular horizontal grid. In each grid cell the median for all occurring events is computed and displayed in color according to the color scheme of the histogram on the right. The red stars indicate the hypocenters of the $M_W$8.1 Iquique event and the $M_W$7.6 largest aftershock for orientation. Underlain are the corresponding coseismic slip distributions in 0.5 m increments taken from Schurr et al. (2014). Two regions of increased stress drop are highlighted by a superimposed black contour line (cf. text). The histogram on the right shows the distribution of stress drops for all 972 target events, with a median of $\overline{\Delta\sigma} = 2.65$ MPa.

with the disappearance of the plate interface seismicity band as described in Sippl et al. (2018). According to them, between 60 km and 80 km depth, the so called upper plane seismicity develops which consists of events which have supposedly different source mechanisms (see Sippl et al. (2018)). We therefore conclude that event depth has no mayor impact on earthquake stress drops in our region, which is in concordance with worldwide observations from Allmann & Shearer (2009) and local earthquake data from New Zealand (Abercrombie et al., 2016). It is in contrast to findings from the Japanese subduction zone (Uchide et al. (2014)), where a strong depth dependence was observed. For northern Chile, Derode & Campos (2019) report evidence for depth dependence of stress drop from 96 events of two different clusters. In their study, however, the velocity spectra are directly fitted with Brune's model, and path effects are not corrected for. We do not observe their reported clear depth dependence of stress drops in our extended data set.

The remaining section in Figure 8 shows the stress drop as a function of event distance from the slab interface. We use the reference model of Hayes et al. (2012) to compute this distance. A roughly symmetrical behavior can be noticed. The interval median at the interface coincides with the overall median. With increasing distance from the interface, the interval median values decrease slightly for several kilometers before they start to increase, both in upward and downward direction. Here, a possible explanation could be the maturity of the rupture surfaces. While close to the interface rupture surfaces have been activated multiply, the intraplate seismicity occurs on more intact fracture zones which produce higher stress drop events. Or, in other terms, the friction coefficient increases when receding from the interface into the plates.

In combination with the previously noted absence of a stress drop dependence with absolute depth this observation suggests that the fault strength and faulting regime play more important roles than the absolute stress.

The long recording period of over 10 years of consistent seismological observations of the northern Chilean subduction zone (IPOC, 2006) also provides a rare opportunity to study the temporal evolution of stress drop. We display the temporal sequence of stress drops in Figure 9 for the time period 2009 to 2017. The data is dominated clearly by the fore- and aftershock seismicity of the 2014 Iquique earthquake. In general, the short time median stress drop varies around the overall median, ranging between 0.6 and 10 MPa. Zooming into the weeks around the Iquique event shows that average values are measured during the two weeks following the large, $M_w$6.6 foreshock. A positive jump of stress

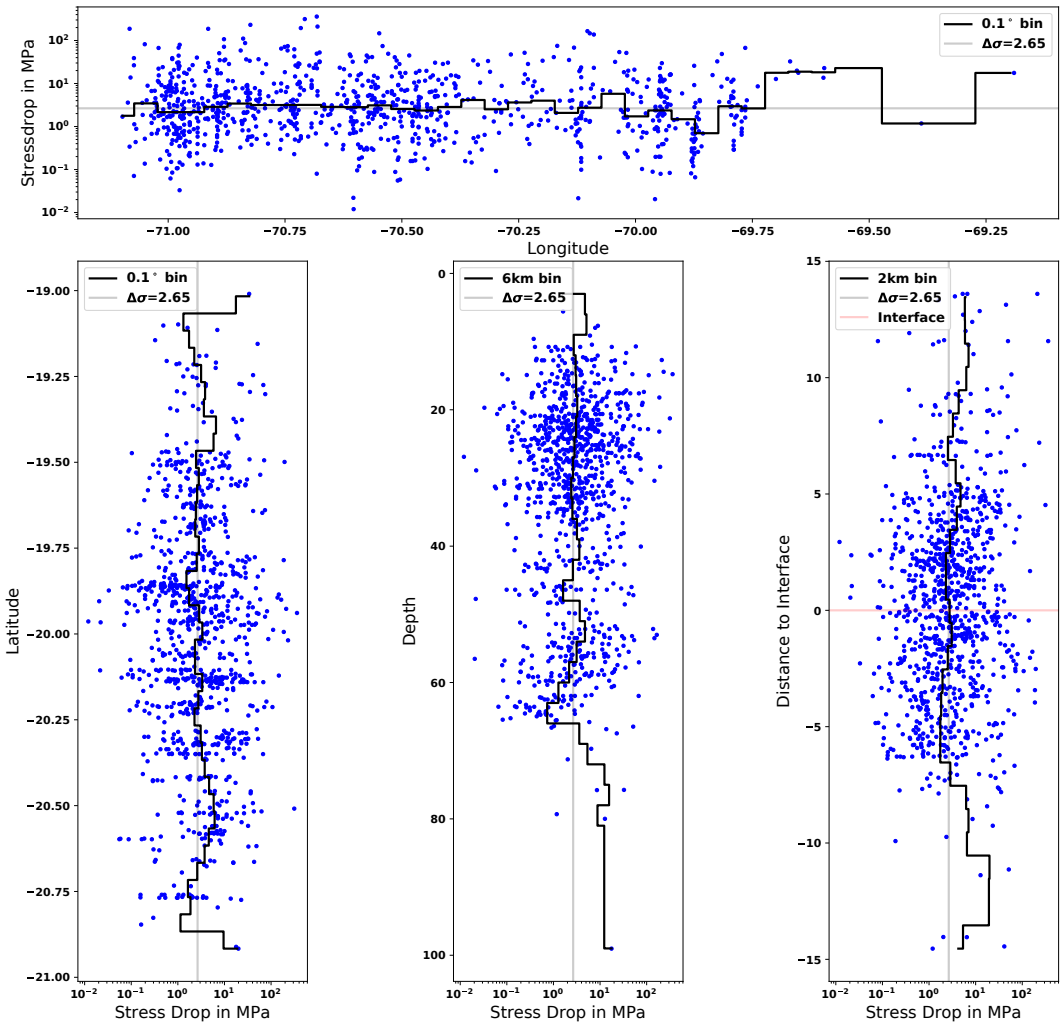


**Figure 8.** Stress drop variation in the spatial domain. The top panel shows stress drop estimates versus easting. The solid line traces the median values for bins of 0.1° width. Below, the stress drop distribution is shown from north to south, against depth and relative to the plate interface from left to right respectively. The binning interval is given in the plot legends. In all plots the median of the entire data set ($\overline{\Delta\sigma}$ = 2.65 MPa) is underlain as a grey line. In the last panel positive distances values refer to events located above the plate interface (red line), negative values to events below it.

drop from 2.7 to about 8 MPa is observed shortly before the mainshock, followed by a steady decrease of stress drop median values down to about 1 MPa over a time interval of 2 to 3 weeks. Then, the trend reverses and the median stress drop rises again to about the average value. Note that the overall median stress drop from before to after the Iquique event decreases from 3.9 MPa to 3.3 MPa, an observation similar to results obtained for events around the 2004 M6.0 Parkfield earthquake hypocenter (Allmann & Shearer, 2007).

We notice that the variation of stress drop in time is not independent of the target event magnitudes that were used to compute the stress drop estimates. In fact, the variation of magnitude is similar to the variation of stress drop. This indicates a correlation of moment and stress drop (Figure 10). To verify the variation of stress drop with time, independent of the given magnitude, we split the events into bins of given magnitudes and analyze them separately. The trend of stress drop increase before and step wise decrease around the Iquique mainshock prevails within each bin. The observed stress drop variation, therefore, is a combination of both effects, a change in stress drop enforced by a change in earthquake moments (for details see supplementary materials, Figures 6 & 7).

The correlation between stress drop and seismic moment was analyzed in many stress drop studies, with diverging results. (Shearer et al., 2006; Abercrombie, 1995) reported moment independent stress drops, whereas several recent studies (in parts of the same groups) observed a relation between stress drop and seismic moment (Abercrombie, 2014; Abercrombie et al., 2016; Trugman & Shearer, 2017). Also, regional differences of this correlation have been reported lately (Trugman & Shearer, 2017). For the northern Chilean subduction zone interface seismicity we observe a clear increase of stress drop with moment. Fitting a standard least square regression line where $log_{10}(\Delta\sigma) = \varepsilon_0 + \varepsilon_1 log_{10}(M_0)$ to the data yields a slope of $\varepsilon_1 = 0.50$ (cf. Figure 10). Such an observation contradicts the self similarity assumption of rupture processes for earthquakes. Still, when compared to other stress drop studies our estimates fall into the typical range between 0.1–100 MPa (Figure 11). However, we observe a smaller decrease of corner frequency with seismic moment than expected for moment independent stress drops. Cocco et al. (2016) gather data from several studies and conclude that while some works show moment dependent stress drops for their particular, limited magnitude ranges the overall picture still shows a self similar rupture behavior with no prevailing dependency of stress drop on moment. Note further that the observation of non-self similarity is made under the assumption

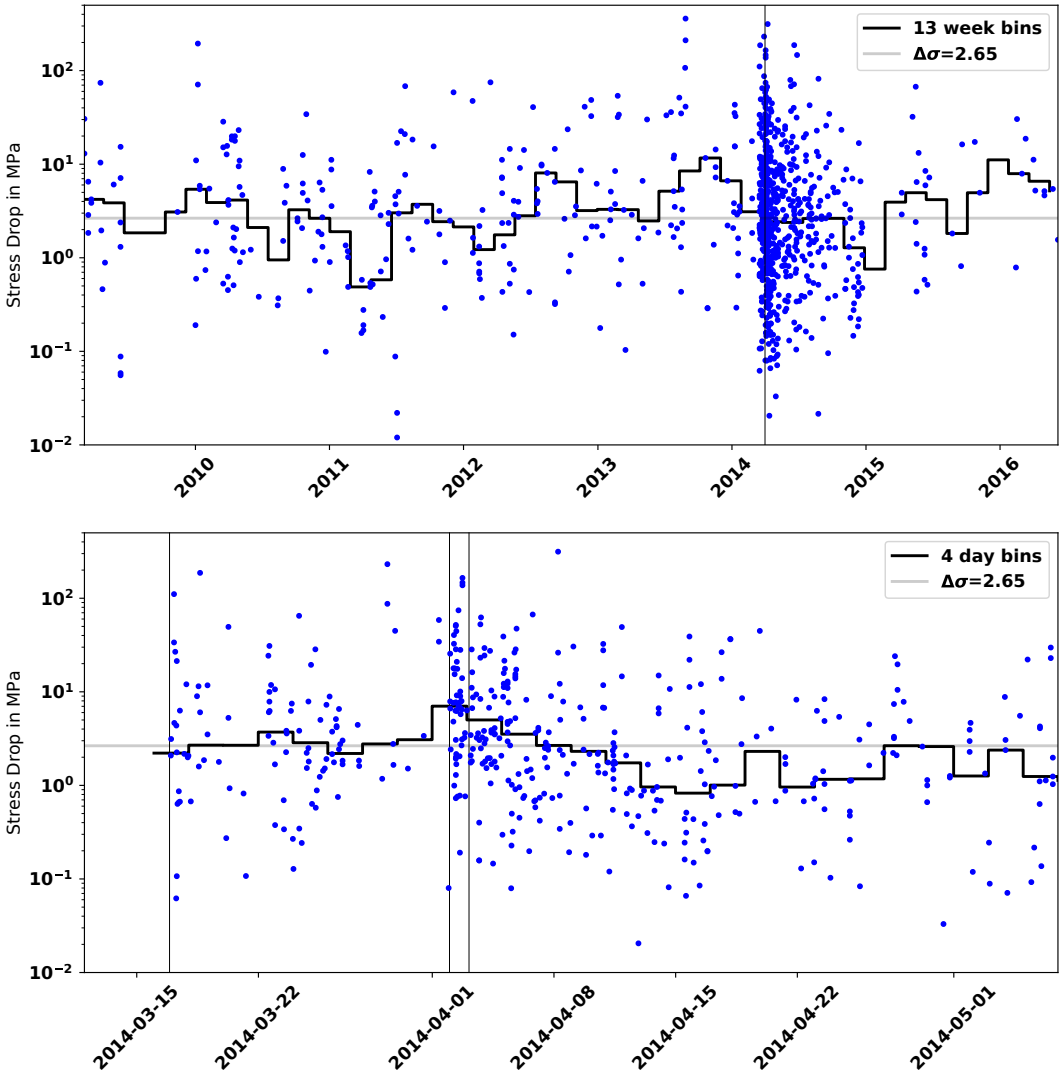


**Figure 9.** Stress drop variation in the time domain. The top panel shows stress drop values for the period from beginning of 2009 to end of 2016. The solid black line traces the median values for bins of 13 weeks time span each. Steps between bins are 8 weeks. Below, a zoom into an eight week time period around the Iquique mainshock is shown starting about two weeks before the event. The three vertical grey lines denote the origin times of the $M_W$6.6 foreshock, the $M_W$8.1 mainshock, and the $M_W$7.6 aftershock. Bin width is four days with two days between steps. In all plots the median of the entire data set ($\overline{\Delta\sigma} = 2.65$ MPa) is underlain as a grey line.

of a fixed value $n = 2$. Trugman & Shearer (2017) point out that for their data self similarity can be obtained by using varied assumptions, e.g. by fitting the spectral model with a different falloff rate.

The procedure described in this article is designed for large data sets where limited knowledge on the events is presumed. As demonstrated by Kaneko & Shearer (2014, 2015) rupture processes may be far more complex than we can assess with current seismological networks. In the case of the IPOC observation system we deal with a one sided observation geometry for most events of this study, and we can only presume that averaging over as many stations as possible provides a reasonable estimate of the corner frequency for a given event. This may be sufficient to extract the more general features which is the main objective of the present study. When conclusions are drawn from particular observations of a small numbers of events, special caution should be taken.

Basically it is possible, albeit out of the scope of this work, to enhance the precision of single event stress drop estimates. For this, the event rupture plane must be known, at best complemented by information on the rupture behavior such as the rupture directivity. For our study area information on fault planes exists (e.g. Cesca et al., 2016; Bloch, Schurr, et al., 2018) and it has been demonstrated that a significant amount of events show rupture directivity (Folesky, Kummerow, Asch, et al., 2018; Folesky, Kummerow, & Shapiro, 2018). The inclusion of such information into our workflow is in principal possible, and it could help in the future to further improve the stress drop estimates.

## Conclusions

The present study introduces our implemented workflow based on the spectral ratio technique and demonstrates its feasibility for the analysis of the northern Chilean subduction zone seismicity.

We compute stress drop estimates for 972 earthquakes in the subduction zone of northern Chile. The events occurred at or close to the plate interface in the rupture region of the 2014 $M_W$8.1 Iquique event. The computed stress drops are log-normal distributed and range mostly from 0.1–100 MPa with a median value of 2.65 MPa. The spatial distribution is heterogeneous, but shows no clear dependence on depth, longitude or latitude. We find, however, a slight increase of median stress drop with distance to the plate interface. We also identify a few small patches of increased stress drop. We ad-

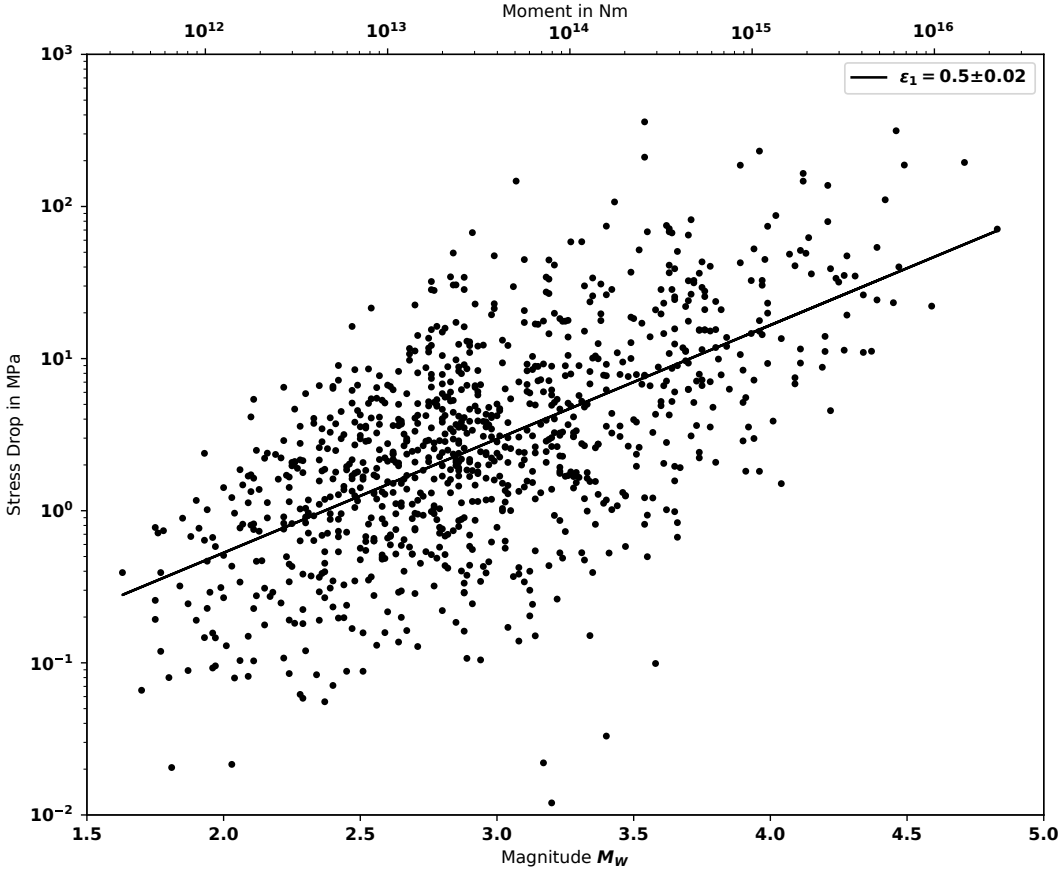


**Figure 10.** Scaling of stress drop with seismic moment. We fit the data with a standard least square regression where $log_{10}(\Delta\sigma) = \varepsilon_0 + \varepsilon_1 log_{10}(M_0)$. The legend gives the result for $\varepsilon_1$ and its standard deviation. A clear dependence of stress drop on seismic moment is observed.

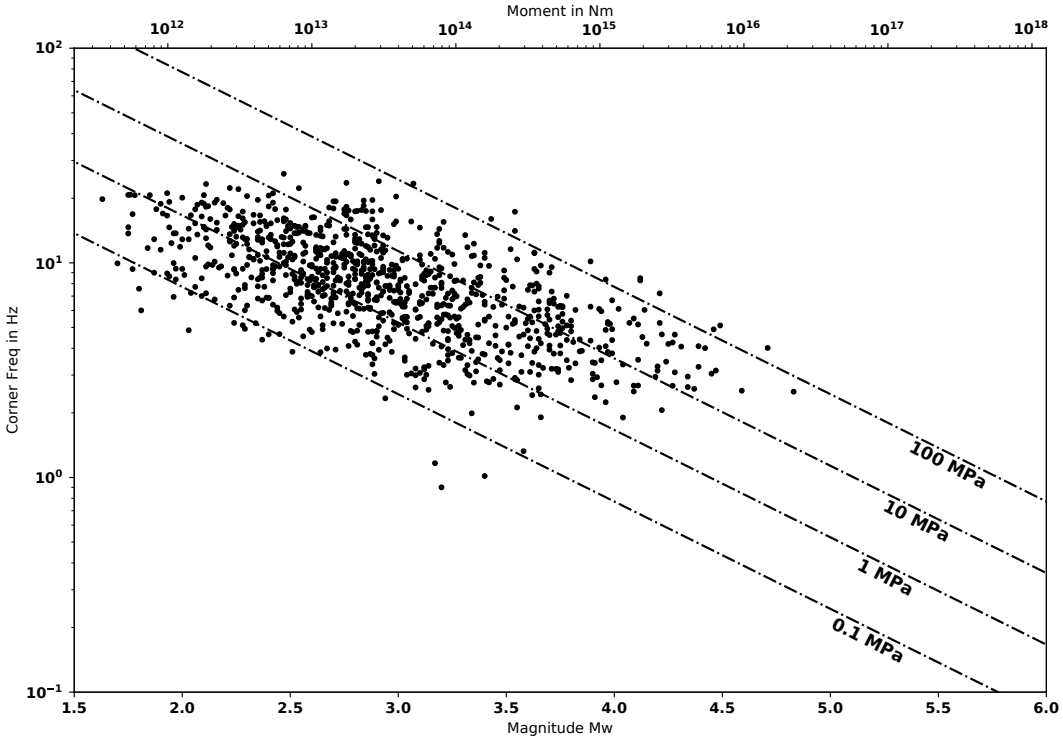


**Figure 11.** Scaling of corner frequency with seismic moment. The dotted lines indicate constant stress drop levels. The great majority of values lie between 0.1 MPa and 100 MPa with a median of $\overline{\Delta\sigma} = 2.65$ MPa. Note that the decrease of corner frequency with magnitude is less than the rate calculated for a moment independence of the stress drops.

ditionally observe a temporal variation of the median stress drop associated with the Iquique megathrust event. Shortly before the event, stress drop increases, followed by a steady decrease lasting for several weeks until the trend reverses and the median stress drop value recovers to the long term average. Furthermore, we find indications that stress drop depends on the seismo-tectonic regime (cf. classification in Sippl et al. (2018)) and that it correlates with the interplate locking.

The stress drop estimates show a clear scaling with seismic moment. We find the empirical relation $log_{10}(\Delta\sigma) = \varepsilon_0 + (0.62 \pm 0.04)\, log_{10}(M_0)$ by fitting a regression line to the data. Therefore, this data set suggests a break of self-similar rupture scaling under the given assumptions.

It is planned to extend the work to the complete data set provided by Sippl et al. (2018) in the near future. Then, not only stress drop estimates for more than the tenfold number of earthquakes will be available, but also events from multiple distinct seismically active regions of the northern Chilean subduction zone will be processed consistently for the first time, potentially allowing for a broader comparative study.

## Data & Resources

Seismograms used in this study were recorded by the seismic CX-net of the Integrated Plate boundary Observatory Chile (IPOC, 2006) using STS-2 broadband seismometers. Data were obtained from the EIDA/GEOPHONE web page (eida.gfz-potsdam.de/webdc3/ or geofon.gfz-potsdam.de/waveform/, accessed on 2017/09/24). Picks, magnitudes and event hypocenter were taken from Sippl et al. (2018). Data processing and figure production were mainly performed using Python3.5.1 (python.org) and packages IPython4.2.0 (Pérez & Granger, 2007), NumPy (Walt et al., 2011), Matplotlib (Hunter, 2007), ObsPy (Beyreuther et al., 2010) and SciPy (Virtanen et al., 2020). Some figures were refined using Inkscape (inkscape.org).

## Acknowledgments

JF was funded by the German Science foundation, DFG, project number KU 2484/2-1, SH 55/15-1. We are grateful to the developers and communities of the utilized open source resources (cf. D&R section) and we thank all institutions that are involved with operating the IPOC network.

## References


Abercrombie, R. E. (1995). Earthquake source scaling relationships from - 1 to 5 ML using seismograms recorded at 2.5 km depth. *Journal of Geophysical Research: Solid Earth*, *100*(B12), 24015–24036.

Abercrombie, R. E. (2014). Stress drops of repeating earthquakes on the San Andreas fault at Parkfield. *Geophysical Research Letters*, *41*(24), 8784–8791.

Abercrombie, R. E. (2015). Investigating uncertainties in empirical Green's function analysis of earthquake source parameters. *Journal of Geophysical Research: Solid Earth*, *120*(6), 4263–4277.

Abercrombie, R. E., Bannister, S., Ristau, J., & Doser, D. (2016). Variability of earthquake stress drop in a subduction setting, the Hikurangi Margin, New Zealand. *Geophysical Journal International*, ggw393.

Allmann, B. P., & Shearer, P. M. (2007). Spatial and temporal stress drop variations in small earthquakes near Parkfield, California. *Journal of Geophysical Research: Solid Earth*, *112*(B4).

Allmann, B. P., & Shearer, P. M. (2009). Global variations of stress drop for moderate to large earthquakes. *Journal of Geophysical Research: Solid Earth*, *114*(B1).

Beyreuther, M., Barsch, R., Krischer, L., Megies, T., Behr, Y., & Wassermann, J. (2010). ObsPy: A Python toolbox for seismology. *Seismological Research Letters*, *81*(3), 530–533.

Bianchi, M., Evans, P. L., Heinloo, A., & Quinteros, J. (2015). *Webdc3 Web Interface.* (GFZ Data Services, doi: 10.5880/GFZ.2.4/2016.001)

Bloch, W., John, T., Kummerow, J., Salazar, P., Krüger, O. S., & Shapiro, S. A. (2018). Watching dehydration: Seismic indication for transient fluid pathways in the oceanic mantle of the subducting Nazca slab. *Geochemistry, Geophysics, Geosystems*, *19*(9), 3189–3207.

Bloch, W., Kummerow, J., Salazar, P., Wigger, P., & Shapiro, S. (2014). High-resolution image of the North Chilean subduction zone: seismicity, reflectivity and fluids. *Geophysical Journal International*, *197*(3), 1744–1749.

Bloch, W., Schurr, B., Kummerow, J., Salazar, P., & Shapiro, S. A. (2018). From slab coupling to slab pull: Stress segmentation in the subducting Nazca plate. *Geophysical Research Letters*, *45*(11), 5407–5416.

Boatwright, J. (1980). A spectral theory for circular seismic sources; Simple estimates of source dimension, dynamic stress drop, and radiated seismic energy. *Bulletin of the Seismological Society of America*, *70*(1), 1–27.

Brune, J. N. (1970). Tectonic stress and the spectra of seismic shear waves from earthquakes. *Journal of Geophysical Research*, *75*(26), 4997. doi: 10.1029/JB075i026p04997

Cesca, S., Grigoli, F., Heimann, S., Dahm, T., Kriegerowski, M., Sobiesiak, M., ... Olcay, M. (2016). The Mw 8.1 2014 Iquique, Chile, seismic sequence: a tale of foreshocks and aftershocks. *Geophysical Journal International*, *204*(3), 1766–1780.

Cocco, M., Tinti, E., & Cirella, A. (2016). On the scale dependence of earthquake stress drop. *Journal of Seismology*, *20*(4), 1151–1170.

Derode, B., & Campos, J. (2019). Energy Budget of Intermediate-Depth Earthquakes in Northern Chile: Comparison With Shallow Earthquakes and Implications of Rupture Velocity Models Used. *Geophysical Research Letters*, *46*(5), 2484–2493.

Eshelby, J. D. (1957). The Determination of the Elastic Field of an Ellipsoidal Inclusion, and Related Problems. In *Proceedings of the royal society of london a: Mathematical, physical and engineering sciences* (Vol. 241, pp. 376–396).

Folesky, J., Kummerow, J., Asch, G., Schurr, B., Sippl, C., Tilmann, F., & Shapiro, S. A. (2018). Estimating Rupture Directions from Local Earthquake Data Using the IPOC Observatory in Northern Chile. *Seismological Research Letters*. doi: 10.1785/0220170202

Folesky, J., Kummerow, J., & Shapiro, S. A. (2018). Patterns of rupture directivity of subduction zone earthquakes in northern Chile. *Journal of Geophysical Research: Solid Earth*, *123*(12), 10–785.

Frankel, A. (1982). The effects of attenuation and site response on the spectra of microearthquakes in the northeastern Caribbean. *Bulletin of the Seismological Society of America*, *72*(4), 1379–1402.

Fuenzalida, A., Schurr, B., Lancieri, M., Sobiesiak, M., & Madariaga, R. (2013). High-resolution relocation and mechanism of aftershocks of the 2007 Tocopilla (Chile) earthquake. *Geophysical Journal International*, *194*(2), 1216–1228.

Goebel, T., Hauksson, E., Shearer, P., & Ampuero, J. (2015). Stress-drop hetero-

geneity within tectonically complex regions: A case study of San Gorgonio Pass, southern California. *Geophysical Journal International*, *202*(1), 514–528.

Hainzl, S., Sippl, C., & Schurr, B. (2019). Linear Relationship Between Aftershock Productivity and Seismic Coupling in the Northern Chile Subduction Zone. *Journal of Geophysical Research: Solid Earth*, *124*(8), 8726-8738. Retrieved from `https://agupubs.onlinelibrary.wiley.com/doi/abs/10.1029/2019JB017764` doi: 10.1029/2019JB017764

Hardebeck, J. L., & Aron, A. (2009). Earthquake stress drops and inferred fault strength on the Hayward fault, east San Francisco Bay, California. *Bulletin of the Seismological Society of America*, *99*(3), 1801–1814.

Hayes, G. P., Herman, M. W., Barnhart, W. D., Furlong, K. P., Riquelme, S., Benz, H. M., ... Samsonov, S. (2014). Continuing megathrust earthquake potential in Chile after the 2014 Iquique earthquake. *Nature*, *512*(7514), 295.

Hayes, G. P., Wald, D. J., & Johnson, R. L. (2012). Slab1. 0: A three-dimensional model of global subduction zone geometries. *Journal of Geophysical Research: Solid Earth*, *117*(B1).

Hoffmann, F., Metzger, S., Moreno, M., Deng, Z., Sippl, C., Ortega-Culaciati, F., & Oncken, O. (2018). Characterizing afterslip and ground displacement rate increase following the 2014 Iquique-Pisagua Mw 8.1 earthquake, Northern Chile. *Journal of Geophysical Research: Solid Earth*, *123*(5), 4171–4192.

Huang, Y., Beroza, G. C., & Ellsworth, W. L. (2016). Stress drop estimates of potentially induced earthquakes in the Guy-Greenbrier sequence. *Journal of Geophysical Research: Solid Earth*, *121*(9), 6597–6607.

Hunter, J. D. (2007). Matplotlib: A 2D graphics environment. *Computing In Science & Engineering*, *9*(3), 90–95.

Hutchings, L., & Viegas, G. (2012). Application of empirical Green's functions in earthquake source, wave propagation and strong ground motion studies. In *Earthquake research and analysis-new frontiers in seismology.* InTech.

IPOC. (2006). *IPOC Seismic Network. Integrated Plate boundary Observatory Chile - IPOC, GFZ German Research Centre for Geosciences; Institut des Sciences de l'Univers-Centre National de la Recherche CNRS-INSU, Seismic Network* (Vol. Seismic Network). (doi: 10.14470/PK615318)

Kanamori, H., & Anderson, D. L. (1975). Theoretical basis of some empirical re-

lations in seismology. *Bulletin of the Seismological Society of America*, *65*, 1073–1095.

Kaneko, Y., & Shearer, P. M. (2014). Seismic source spectra and estimated stress drop derived from cohesive-zone models of circular subshear rupture. *Geophysical Journal International*, *197*(2), 1002–1015. doi: 10.1093/gji/ggu030

Kaneko, Y., & Shearer, P. M. (2015). Variability of seismic source spectra, estimated stress drop, and radiated energy, derived from cohesive-zone models of symmetrical and asymmetrical circular and elliptical ruptures. *Journal of Geophysical Research B: Solid Earth*, *120*(2), 1053–1079. doi: 10.1002/2014JB011642

Konno, K., & Ohmachi, T. (1998). Ground-motion characteristics estimated from spectral ratio between horizontal and vertical components of microtremor. *Bulletin of the Seismological Society of America*, *88*(1), 228–241.

Lancieri, M., Madariaga, R., & Bonilla, F. (2012). Spectral scaling of the aftershocks of the Tocopilla 2007 earthquake in northern Chile. *Geophysical Journal International*, *189*(1), 469–480.

Li, S., Moreno, M., Bedford, J., Rosenau, M., & Oncken, O. (2015). Revisiting viscoelastic effects on interseismic deformation and locking degree: A case study of the peru-north chile subduction zone. *Journal of Geophysical Research: Solid Earth*, *120*(6), 4522–4538.

Madariaga, R. (1976). Dynamics of an expanding circular fault. *Bulletin of the Seismological Society of America*, *66*(3), 639–666.

Menke, W. (1999). Using waveform similarity to constrain earthquake locations. *Bulletin of the Seismological Society of America*, *89*(4), 1143–1146.

Moreno, M., Li, S., Melnick, D., Bedford, J., Baez, J., Motagh, M., ... others (2018). Chilean megathrust earthquake recurrence linked to frictional contrast at depth. *Nature Geoscience*, *11*(4), 285–290.

Moreno, M., Metzger, S., Bedford, J., Hoffmann, F., Li, S., Deng, Z., ... Oncken, O. (2016). Satellitengeodäsie und Erdbebendeformation in der nordchilenischen seismischen lücke. *System Erde*, *6*(2), 36–41.

Mueller, C. S. (1985). Source pulse enhancementt by deconvolution of an empirical Green's function. *Geophys. Res. Lett.*, *12*, 33–36.

Münchmeyer, J., Bindi, D., Sippl, C., Leser, U., & Tilmann, F. (2020). Low uncertainty multifeature magnitude estimation with 3-D corrections and boosting tree

regression: application to North Chile. *Geophysical Journal International*, *220*(1), 142–159.

Pérez, F., & Granger, B. E. (2007). Ipython: a system for interactive scientific computing. *Computing in Science & Engineering*, *9*(3).

Prieto, G. A., Shearer, P. M., Vernon, F. L., & Kilb, D. (2004). Earthquake source scaling and self-similarity estimation from stacking P and S spectra. *Journal of Geophysical Research: Solid Earth*, *109*(B8).

Ruiz, S., Metois, M., Fuenzalida, A., Ruiz, J., Leyton, F., Grandin, R., ... Campos, J. (2014). Intense foreshocks and a slow slip event preceded the 2014 Iquique Mw 8.1 earthquake. *Science*, *345*(6201), 1165–1169.

Sato, T., & Hirasawa, T. (1973). Body wave spectra from propagating shear cracks. *Journal of Physics of the Earth*, *21*(4), 415–431.

Schurr, B., Asch, G., Hainzl, S., Bedford, J., Hoechner, A., Palo, M., ... others (2014). Gradual unlocking of plate boundary controlled initiation of the 2014 Iquique earthquake. *Nature*, *512*(7514), 299.

Schurr, B., Asch, G., Rosenau, M., Wang, R., Oncken, O., Barrientos, S., ... Vilotte, J.-P. (2012). The 2007 m7. 7 Tocopilla northern Chile earthquake sequence: Implications for along-strike and downdip rupture segmentation and megathrust frictional behavior. *Journal of Geophysical Research: Solid Earth*, *117*(B5).

Shearer, P. M., Abercrombie, R. E., Trugman, D. T., & Wang, W. (2019). Comparing EGF methods for estimating corner frequency and stress drop from P wave spectra. *Journal of Geophysical Research: Solid Earth*, *124*(4), 3966–3986.

Shearer, P. M., Prieto, G. A., & Hauksson, E. (2006). Comprehensive analysis of earthquake source spectra in southern California. *Journal of Geophysical Research: Solid Earth*, *111*(B6).

Sibson, R. H. (1974). Frictional constraints on thrust, wrench and normal faults. *Nature*, *249*(5457), 542–544.

Sippl, C., Schurr, B., Asch, G., & Kummerow, J. (2018). Seismicity structure of the Northern Chile forearc from >100,000 double-difference relocated hypocenters. *Journal of Geophysical Research: Solid Earth*, *123*. doi: doi:10.1002/2017JB015384

Trugman, D. T., & Shearer, P. M. (2017). Application of an improved spectral de-

composition method to examine earthquake source scaling in Southern California. *Journal of Geophysical Research: Solid Earth*, *122*(4), 2890–2910.

Uchide, T., Shearer, P. M., & Imanishi, K. (2014). Stress drop variations among small earthquakes before the 2011 Tohoku-oki, Japan, earthquake and implications for the main shock. *Journal of Geophysical Research: Solid Earth*, *119*(9), 7164–7174.

Venkataraman, A., & Kanamori, H. (2004). Observational constraints on the fracture energy of subduction zone earthquakes. *Journal of Geophysical Research: Solid Earth*, *109*(B5).

Virtanen, P., Gommers, R., Oliphant, T. E., Haberland, M., Reddy, T., Cournapeau, D., ... others (2020). Scipy 1.0: fundamental algorithms for scientific computing in Python. *Nature methods*, 1–12.

Walt, S. v. d., Colbert, S. C., & Varoquaux, G. (2011). The NumPy array: a structure for efficient numerical computation. *Computing in Science & Engineering*, *13*(2), 22–30.

Ye, L., Lay, T., Kanamori, H., & Rivera, L. (2016). Rupture characteristics of major and great (Mw$\geq$ 7.0) megathrust earthquakes from 1990 to 2015: 1. source parameter scaling relationships. *Journal of Geophysical Research: Solid Earth*, *121*(2), 826–844.